PCCP

PAPER

View Article Online
View Journal | View Issue

Check for updates

Cite this: *Phys. Chem. Chem. Phys.*, 2024, **26**, 21229

Effect of cholesterol on nanoparticle translocation across a lipid bilayer†

Masaya Tajima, Hideya Nakamura,* Shuji Ohsaki and Satoru Watano

Received 24th January 2024,
Accepted 19th July 2024

DOI: 10.1039/d4cp00330f

rsc.li/pccp

Nanoparticles (NPs) have attracted significant attention as carriers for the delivery of drugs, genes, and macromolecules for biomedical and therapeutic applications. These technologies require NPs to be delivered to the interior of the cell. However, this translocation is unlikely because of the presence of a cell membrane composed of phospholipids, cholesterol, proteins, and glycans. The cell membrane composition can influence its rigidity; thus, membrane composition is a crucial factor in determining the translocation of NPs across the cell membrane. Here, we focus on cholesterol, which is an essential component of biological cell membranes, and investigate NP translocation across membranes containing cholesterol under an applied electric field using a coarse-grained molecular dynamics simulation. We found that NPs could translocate directly across cholesterol-containing membranes without irreversible membrane disruption. This unique translocation was induced by two key phenomena. Before NP translocation, a phospholipid-rich/cholesterol-poor domain was formed at the NP–membrane contact interface. Second, a smaller transmembrane pore was formed in the cholesterol-containing membrane during membrane crossing of the NP. Our findings imply that the delivery of NPs to the cell interior across the cholesterol-containing membrane can be achieved by appropriately controlling the strength of the applied electric field, depending on the cholesterol content in the membrane.

Open Access Article. Published on 24 July 2024. Downloaded on 5/24/2026 4:01:49 PM.
This article is licensed under a Creative Commons Attribution 3.0 Unported Licence.

Introduction

Nanoparticles (NPs) have gained considerable attention as pivotal materials for next-generation biomedical and therapeutic technologies. Owing to their unique physicochemical properties resulting from their small size and large specific surface area, NPs offer various potential applications in drug, gene, and macromolecule delivery;[1–5] magnetic hyperthermia; photothermal therapy;[6] radiotherapy;[7] and bioimaging.[8,9] Furthermore, the integration of therapeutic and diagnostic techniques using NPs, known as theranostics, has emerged as an attractive strategy for treating cancers and tumors.[10,11] These technologies require the delivery of NPs into the cell and their transportation to the target cellular components without damaging the cells. The cell membrane serves as a major biological barrier during NP delivery and transport. Therefore, it is crucial to have a fundamental understanding of NP translocation across the cell membrane and how it can be controlled for successful biomedical and therapeutic application of NPs.

It has been found that NPs can translocate across the membrane through two main pathways:[12–14] endocytosis and direct translocation. Endocytosis, recognized as a major translocation pathway, involves the NP being wrapped and enclosed by a portion of the cell membrane and then internalized into the cell by an endocytic vesicle. However, NPs enclosed within a vesicle often encounter difficulties in escaping from the vesicle, resulting in uncontrolled cellular trafficking and low delivery efficiency.[12] In contrast, direct translocation is a non-endocytic pathway in which an NP directly reaches the cytoplasm without being enclosed by endocytic vesicles, resulting in high delivery efficiency. However, direct translocation is less likely than endocytosis.[12] Therefore, a key challenge for the success of biomedical and therapeutic applications of NPs is the development of new technologies that can induce direct translocation.

Physical methods in which cells are exposed to external forces have been used to deliver extracellular objects into cells *via* the direct translocation pathway. One of the most commonly used physical methods is electroporation, in which a high-intensity electric field is applied to the cells.[15] The external electric field induces transient defects and pores in the cell membrane, facilitating the direct translocation of extracellular objects into the cell. Electroporation has also been used to deliver NPs, resulting in a significant enhancement in delivery efficacy.[16–18] A previous study indicated that electroporation treatment shifts the dominant pathway of NP intracellular delivery from endocytosis to direct translocation without entrapment in an endocytic vesicle.[16] However, a notable concern

Department of Chemical Engineering, Osaka Metropolitan University, 1-1 Gakuen-cho, Naka-ku, Sakai, Osaka 599–8531, Japan. E-mail: hideyanakamura@omu.ac.jp

† Electronic supplementary information (ESI) available. See DOI: https://doi.org/10.1039/d4cp00330f

Open Access Article. Published on 24 July 2024. Downloaded on 5/24/2026 4:01:49 PM. This article is licensed under a Creative Commons Attribution 3.0 Unported Licence.

with electroporation is the potential risk of high cellular mortality resulting from the cells being subjected to excess stress from an external electric field.

We investigated the translocation of a charged NP across a phospholipid bilayer (model cell membrane) under an electric field using molecular dynamics (MD) simulation[19–21] and experiments using a planar bilayer membrane.[22] Our MD simulations revealed that even under a weak external electric field below the membrane breakdown intensity, the charged NP was directly translocated across a model cell membrane without membrane disruption.[19–21] The applied electric field that induced this unique direct translocation pathway was significantly lower than that used in conventional electroporation. This unique direct translocation pathway offers a distinct advantage over translocation pathways induced by conventional electroporation. Our research also revealed that this direct translocation can be triggered by a locally enhanced membrane potential induced at the NP–membrane contact interface.[20] We also demonstrated this translocation pathway in an experiment using an artificial planar bilayer membrane and an electrophysiological technique.[22] However, the NP translocation pathway has not yet been sufficiently examined. One less explored aspect is the composition of the cell membrane. Our previous studies employed a simple cell membrane model consisting solely of phospholipids, whereas the actual plasma cell membrane consists of phospholipids and other constituent molecules such as cholesterol and proteins. Among these constituent molecules, except for phospholipids, cholesterol is the most prevalent, accounting for 40–50 mol% of the plasma cell membrane.[23,24] Cholesterol is also recognized as an important molecule that regulates the fluidity and rigidity of plasma cell membranes by increasing the packing density of lipid molecules.[25,26]

Understanding the influence of cholesterol on membrane stability and permeability is important in many fields related to cell membranes. MD simulation[27] and experimental studies[28,29] have reported that cholesterol-containing phospholipid bilayers are more likely to maintain their structure compared to cholesterol-free bilayers, even under a high electric field. Several MD simulation studies have investigated the influence of cholesterol on the membrane permeability of drug molecules and amino acids using thermodynamic analysis. Yuan and Meng revealed that the translocation of chlorzoxazone across the cell membrane was inhibited at a higher cholesterol content, which was attributed to the formation of hydrogen bonds between cholesterol and phospholipoid head groups.[30] Zhang *et al.* found that the energy required for the membrane crossing of doxorubicin increased in the presence of cholesterol, whereas the energy required for the membrane crossing of ellipticine remained unchanged, even in the presence of cholesterol.[31] This difference was due to the different hydrogen bonding behaviors between each drug and the lipid molecule. De Sá *et al.* reported that the free energy barrier for membrane crossing of miltefosine was the highest in a DPPC bilayer containing 30 mol% cholesterol.[32] Chen *et al.* revealed that an increase in cholesterol content causes a transition in the ion permeation mechanism.[33] With an increase in membrane thickness derived from a higher cholesterol content, the ion-induced defect permeation mechanism, where significant membrane deformation accompanies ion permeation, shifted to the solubility-diffusion mechanism, where ions penetrate the membrane with large associated dehydration energy costs.[33] Gkeka *et al.* performed MD simulations and investigated the interactions between anionic NPs and cholesterol-containing DPPC bilayers when the NPs were artificially inserted into the bilayer core.[34] The results revealed that the inserted NPs reduced the cholesterol concentration in their vicinity, suggesting that the membrane composition in the vicinity of the NPs could change. They also suggested that this change in the local membrane composition could alter the membrane permeability of NPs.

In the aforementioned studies, the permeability of small substances and anionic NPs through cholesterol-containing membranes was computationally investigated from a thermodynamic perspective. However, the previous MD simulation studies were performed with ''biased'' MD simulations, where substances or NPs were artificially forced to translocate across the membrane. However, this approach does not reflect the actual NP dynamics of direct translocation across the membrane. Furthermore, previous studies have not investigated membrane permeability in the presence of an external electric field.

In this study, with an ''unbiased'' MD simulation, we investigated for the first time the direct translocation of a cationic NP across a cholesterol-containing lipid bilayer under an external electric field. First, the influence of cholesterol content on the critical applied electric potential for membrane breakdown was investigated using MD simulations. Second, the translocation of the NP across the cholesterol-containing membrane was investigated under various cholesterol contents and intensities of applied membrane potential, and the influence of cholesterol content on the membrane-crossing behavior of the NP was discussed. Finally, the lipid composition at the NP–membrane contact interface and the size of the transmembrane pore during NP translocation were analyzed as key phenomena in NP translocation.

Simulation method

Coarse-grained MD simulation

The MD simulations were performed using a coarse-grained (CG) model. The interactions between the CG molecular sites were modeled using the MARTINI force field.[35,36] The MARTINI force field has been validated in various systems, including biomembranes.[37–39] Yesylevskyy *et al.* compared the MARTINI force field with an all-atomistic force field in terms of the critical intensity of the electric field for electroporation and verifying good agreement.[39] Fig. 1a illustrates the initial configuration of the simulation system used in this study. The system is mainly composed of double lipid bilayers, two solvent compartments, and a single NP.[19–21] As for lipid

 This journal is © the Owner Societies 2024

Open Access Article. Published on 24 July 2024. Downloaded on 5/24/2026 4:01:49 PM.
This article is licensed under a Creative Commons Attribution 3.0 Unported Licence.

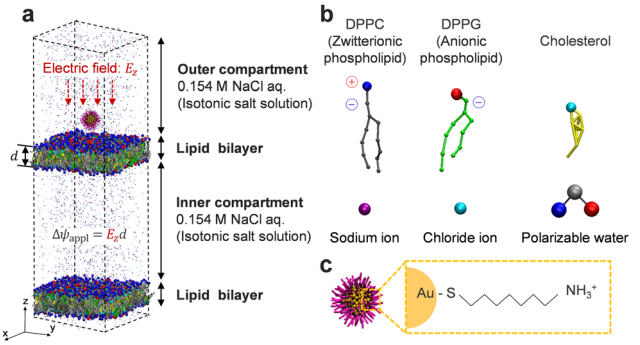

Fig. 1 Simulation system used in this study. (a) Initial configuration. Water molecules are not displayed for clarity. (b) Snapshots of individual CG molecules. (c) Snapshots of a positively charged 8-amino-1-octanethiol-coated gold NP.

molecules, coarse-grained DPPC[35] (1,2-dipalmitoylphosphatidylcholine), DPPG[38] (1,2-dipalmitoylphosphatidylglycerol), and cholesterol[40] were employed (Fig. 1b). The head groups of DPPC and DPPG are zwitterionic and anionic, respectively. Coarse-grained cholesterol is composed of a non-charged hydroxyl group, a rigid steroid group, and a hydrocarbon tail. The rigidity of the steroid group was modeled using virtual interaction sites.[40] The phospholipid bilayer used in this study was negatively charged, mimicking the negatively charged characteristics of plasma cell membranes.[41] CG sodium and chloride ions[35] and a polarizable water model[39] in the MARTINI force field were used as the solvent molecules (Fig. 1b). For the NP (Fig. 1c), a cationic gold NP coated with 8-amino-1-octanethiol (amino-OT) was used.[21–23] This NP is typically used in biomedical and pharmaceutical applications.[42] Amino-OT contains a positively charged amine terminal. The core gold cluster was composed of 314 gold atoms with an FCC lattice structure and a truncated octahedral morphology. The binding sites of the amino-OTs with the core gold cluster were preliminarily calculated using atomistic MD simulations.[19] The atomistic amino-OT-coated gold NP was then coarse-grained according to the MARTINI force-field in the same manner as in previous studies.[19,43,44] Force field parameters, which were developed in previous studies[19,43,44] and compatible with a MARTINI force-field, were employed for the NP used in this study. After a series of pre-calculations, the NP coated with 120 amino-OTs was finally obtained, resulting in a total NP charge of +120*e*. The diameters and surface charge densities of the NP were 3.9 nm and 2.51 e nm^{-2}, respectively. The surface charge density corresponds to an NP surface potential of 25.7 mV at a Debye length of 154 mM NaCl (aq), as estimated using Ohshima's equation.[45]

Simulation system

The double-lipid bilayer system used in this study was designed to provide two independent solvent compartments (Fig. 1a). The NaCl concentration in each solvent compartment was set to 154 mM, which is equivalent to the concentration of the isotonic saline solution. The numbers of coarse-grained sites in the simulation systems used in this study are listed in Table 1. To offset the negative charge of DPPG and maintain electroneutrality in each solvent compartment, sodium ions were added to the base condition (154 mM NaCl aq.). The NP was then placed in the outer solvent compartment. To offset the positive charge of the NP (+120 e) and maintain electroneutrality in the outer solvent compartment, 120 chloride ions were also concurrently added to the outer solvent compartment. The molecular compositions used in this study ensured no ionic imbalance or osmotic pressure across the lipid bilayers. The cholesterol content of the membrane was varied from 0 to 50 mol%. This corresponds to the typical cholesterol content in mammalian cell membranes.[23,24] The size of the simulation system was set as 18 × 18 × 60 nm.

To investigate the influence of cholesterol, phospholipid bilayer systems with various cholesterol contents were constructed. The construction procedure is as follows.[46] First, from a fully equilibrated DPPC–DPPG bilayer system,[19,20] DPPC and DPPG molecules were randomly selected and replaced with cholesterol molecules. In this replacement, the position of the cholesterol molecules in the in-plane direction of the membrane was set to match that of the selected DPPC or DPPG, whereas the position of the OH group of the cholesterol molecules in the membrane's normal direction was set to 0.52 nm inside the membrane from the phosphate group of the selected DPPC or DPPG. The depth (0.52 nm) was determined from a previous simulation study.[47] Second, the orientation of the inserted cholesterol molecules was optimized. Each cholesterol molecule was rotated 15° in 24 steps around the normal membrane axis. For each 15° rotation, the intermolecular potential between cholesterol and the adjacent DPPC and DPPG molecules was calculated. The optimal angle for the

Table 1 Molecular compositions of the simulation systems in this study

Cholesterol content [mol%]	0	10	20	30	40	50
DPPC	1936	1740	1548	1356	1164	968
DPPG	368	332	296	256	220	184
Cholesterol	0	232	460	692	920	1152
Water	123 586	123 586	123 586	123 586	123 586	123 586
Nanoparticle (NP)	1	1	1	1	1	1
Sodium ion in the inner compartment (with and without NP)	894	876	858	838	820	802
Sodium ion in the outer compartment (with and without NP)	894	876	858	838	820	802
Chloride ion in the inner compartment (with and without NP)	710	710	710	710	710	710
Chloride ion in the outer compartment (without NP)	710	710	710	710	710	710
Chloride ion in the outer compartment (with NP)	830	830	830	830	830	830

Open Access Article. Published on 24 July 2024. Downloaded on 5/24/2026 4:01:49 PM. This article is licensed under a Creative Commons Attribution 3.0 Unported Licence.

inserted cholesterol molecule was set to the smallest intermolecular potential. Finally, MD simulations were performed to equilibrate the cholesterol-containing membranes. To gradually equilibrate the entire system, an equilibrium simulation was performed with artificially reduced van der Waals parameters of cholesterol.[46] Once the system was equilibrated with the reduced van der Waals parameters in the NPT ensemble at 310 K and 1 bar, stepwise increases in the reduced van der Waals parameters and the subsequent equilibration calculations were repeated.[46] This procedure was repeated until the van der Waals parameters reached their original values.

External electric field

To consider the external electric field E in the MD simulation, the force $F_e = q_iE$ was added to all CG sites with a charge q_i.[48] E was applied downward along the negative z-axis and perpendicular to the membrane surface, generating an electric potential difference across the membrane. This resulting potential difference was defined as the applied membrane potential $\Delta\psi_{appl}$. $\Delta\psi_{appl}$ was calculated as $\Delta\psi_{appl} = |E|d$, where d is the thickness of the membrane. E was treated as a run parameter for the CG-MD simulation. d was obtained from our CG-MD simulation results for the fully equilibrated cholesterol-containing membranes. Table 2 lists the calculated d. The increase in d at higher cholesterol contents was attributed to the condensing effect of cholesterol.[49,50] In this study, the simulations were conducted under a weak $\Delta\psi_{appl}$, which was lower than the membrane breakdown potential referred to as $\Delta\psi_{appl,C}$.

Simulation conditions

All simulations were performed using the GROMACS 4.0.7 package.[51] The simulation results were visualized using the Visual Molecular Dynamics 1.9.3 package.[52] For simulations of a cholesterol-containing membrane and solvents without NP and electric field, the MD simulation was performed using the NPT ensemble. For simulations of a cholesterol-containing membrane with NP under an electric field, the MD simulations were performed using the NPzAT ensemble, in which the temperature, membrane area, and pressure along the membrane normal were maintained constant.[19–21] The pressure was maintained at 1 bar using the Parrinello–Rahman pressure coupling method,[53] with a time constant of 12 ps and a compressibility of 3×10^{-4} bar^{-1}. The temperature was maintained at 310 K using a velocity rescaling method.[54] The electrostatic interactions were calculated using the particle mesh Ewald method with a real-space cutoff length of 1.2 nm and a fast Fourier-transform grid spacing of 0.24 nm. The relative dielectric constant was set to 2.5, which was a requirement of the polarizable water model[39] used in this study. The Lennard-Jones potentials for the van der Waals interactions were calculated within a cutoff length of 1.2 nm. Periodic boundary conditions were applied in all the directions. In the initial configuration, the NP was placed above the outer surface of the upper lipid bilayer. The dynamics of all the molecules and NP under an applied electric field (E) were then simulated for 200 ns. The lower lipid bilayer was constrained during the MD simulation to prevent the permeation of water and ions across it. Five independent simulation runs were performed at different initial lateral positions of the NP to evaluate the occurrence probabilities of the NP behavior.

In this study, MD simulations for NP–membrane interactions under an electric field were performed under the NPzAT ensemble, in which the membrane area was constant. This was necessary due to the presence of an electric field to avoid a major artifact in the simulation that could lead to an unrealistic change in the membrane area. Nevertheless, this constant-area treatment raised a concern about whether the interaction between the NP and the membrane can be simulated without a change in the membrane area, which can be caused by the interaction between the NP and the membrane. Thus, we preliminarily investigated the lateral membrane pressure when the NP–membrane interaction events (*e.g.*, adhesion, penetration, and translocation) occurred under the electric field and NPzAT ensemble. Consequently, the lateral pressure did not change significantly even when the NP adhered to the membrane and translocated across the membrane (for details, please see Fig. S3 in the ESI†). These results indicate that the influence of the NP–membrane interaction events on the membrane lateral pressure was almost negligible in the case of our simulation conditions. Thus, in this study, we considered that the interaction between the NP and the membrane can be simulated even with the NPzAT ensemble. We expected that the influence of NP–membrane interaction events on the lateral pressure could be significant in the case of much larger membrane deformation, for example, in the case of membrane wrapping and vesiculation with a much larger NP.

Table 2 Membrane thickness d as a function of cholesterol content

Cholesterol contents [mol%]	0	10	20	30	40	50
Membrane thickness d [nm]	3.81	3.92	4.03	4.18	4.30	4.35

Results and discussion

Effect of cholesterol on membrane properties

To investigate the effect of cholesterol on the membrane properties, we conducted MD simulations of an equilibrated system composed of a cholesterol-containing membrane and solvents without NP and an electric field. In this investigation, the NPT ensemble was applied.

To verify the CG-MD simulations in this study, the results were compared with those of previous all-atomistic MD simulations.[35,55] We calculated the area per lipid (A_{lipid})[35,55] to measure the membrane packing density. A_{lipid} was the average surface area occupied by a single lipid molecule in a membrane. A_{lipid} was calculated as $A_{lipid} = 4L_xL_y/N_{lipid}$, where L_x and L_y are the lengths of the simulation system in the x- and y-directions (in-plane direction), respectively, and N_{lipid} denotes the total number of molecules comprising the double lipid bilayers (*i.e.*, DPPC, DPPG, and cholesterol). $\langle\rangle$ denotes the

 This journal is © the Owner Societies 2024

Open Access Article. Published on 24 July 2024. Downloaded on 5/24/2026 4:01:49 PM.
This article is licensed under a Creative Commons Attribution 3.0 Unported Licence.

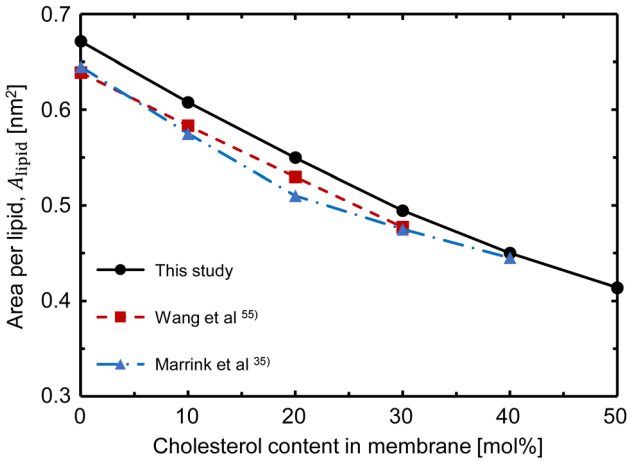

Fig. 2 Area per lipid (A_{lipid}) as a function of cholesterol content in the membrane. Lipid molecules were DPPC, DPPG, and cholesterol in this study.

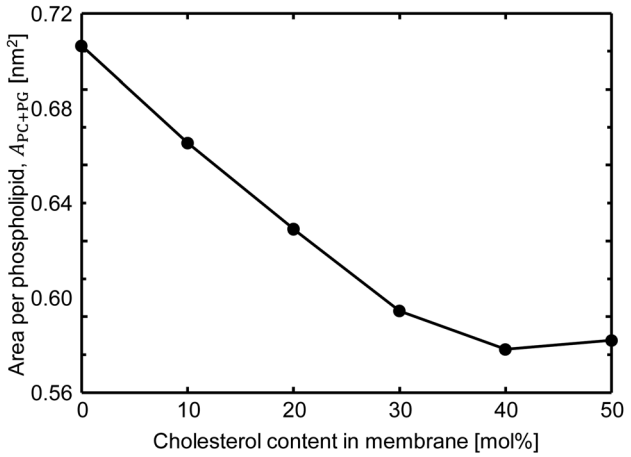

Fig. 3 Critical applied potential for membrane breakdown ($\Delta\psi_{appl,C}$) as a function of cholesterol content in the membrane.

ensemble average of values within $\langle\rangle$. Fig. 2 shows A_{lipid} as a function of cholesterol content. A_{lipid} decreased with increasing cholesterol content, indicating the typical condensing effect of cholesterol in the lipid bilayer. The A_{lipid} values calculated in this study were in agreement with those calculated in all-atomistic MD simulations,[35,55] verifying the CG-MD simulation in this study.

The effect of the cholesterol content on the critical applied potential for membrane breakdown ($\Delta\psi_{appl,C}$) was then investigated. $\Delta\psi_{appl,C}$ was defined as the minimum $\Delta\psi_{appl}$ at which the membrane was irreversibly disrupted. To determine $\Delta\psi_{appl,C}$, CG-MD simulations were performed by applying various intensities of $\Delta\psi_{appl}$ for 200 ns to a simulation system consisting of the membranes and solvents without NP. The critical $\Delta\psi_{appl}$, at which the permanent transmembrane pore emerged, was defined as $\Delta\psi_{appl,C}$. Fig. 3 shows the relationship between the cholesterol content in the membrane and $\Delta\psi_{appl,C}$. $\Delta\psi_{appl,C}$ increased as the cholesterol content increased up to 30 mol%, whereas there was little change in $\Delta\psi_{appl,C}$ over 30 mol%. This non-monotonic trend in $\Delta\psi_{appl,C}$ with respect to the cholesterol content was consistent with the results of experimental studies.[29,56] The increase in $\Delta\psi_{appl,C}$ up to 30 mol% cholesterol was due to the tight packing of lipid molecules derived from the cholesterol condensing effect.[49,50] This was confirmed by a decrease in A_{lipid} up to 30 mol% cholesterol, as shown in Fig. 2. However, A_{lipid} in Fig. 2 did not provide a reasonable explanation for the unchanged $\Delta\psi_{appl,C}$ over 30 mol% of cholesterol content, because A_{lipid} decreased even over 30 mol% of the cholesterol content. To compensate for this gap, the area per phospholipid (A_{PC+PG}) was calculated. A_{PC+PG} corresponds to the average surface area per phospholipid (DPPC and DPPG) in the membrane. A_{PC+PG} exhibited only a cholesterol-condensing effect on phospholipid molecules. A_{PC+PG} was calculated using the following equation:[57]

$$A_{PC+PG} = \left\langle \frac{4L_xL_y}{N_{PC+PG}} \right\rangle \left(1 - \frac{V_{Chol}}{V_{mem}}\right) = \left\langle \frac{4L_xL_y}{N_{PC+PG}} \right\rangle \left(1 - \frac{V_{Chol}}{V_{sys} - V_{sol}}\right) \quad (1)$$

where N_{PC+PG} is the total number of phospholipid molecules (DPPC and DPPG). V_{Chol}, V_{mem}, V_{sys}, and V_{sol} are the volumes of the whole cholesterol, whole membrane, whole simulation system, and whole solvent compartments, respectively. To calculate V_{Chol}, we used a volume of 0.593 nm^3 per cholesterol molecule[46] and multiplied it by the number of cholesterol molecules. To calculate V_{sol}, we used the water slab volume obtained from the CG-MD simulation using the MARTINI force field and the ion volume from the literature.[58] Fig. 4 shows A_{PC+PG} as a function of cholesterol content. A_{PC+PG} decreased as the cholesterol content increased, whereas A_{PC+PG} remained almost unchanged over 30 mol% cholesterol. This result suggests that the cholesterol-condensing effect on phospholipid molecules was saturated at a cholesterol content of over 30 mol%. This saturation led to the unchanged $\Delta\psi_{appl,C}$ at a cholesterol content of over 30 mol%.

Direct translocation of the NP across a cholesterol-containing lipid bilayer under an external electric field

Interaction between the NP and the lipid bilayer containing cholesterols under various applied membrane potentials

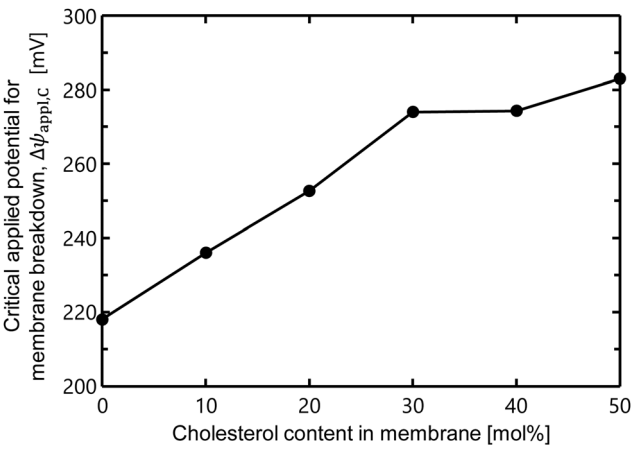

Fig. 4 Area per phospholipid (A_{PC+PG}) as a function of cholesterol content in the membrane.

Open Access Article. Published on 24 July 2024. Downloaded on 5/24/2026 4:01:49 PM.
This article is licensed under a Creative Commons Attribution 3.0 Unported Licence.

($\Delta\psi_{appl}$) was investigated with a simulation system composed of the double lipid bilayers, solvents, and NP. The NP behavior under various conditions can be classified into three modes, as shown in Fig. 5a: NP adhesion to the outer surface of the membrane (mode I), NP translocation with self-resealing of the pore (mode II), and NP translocation with persistent porosity (mode III). In mode I, the positively charged NP adhered to the surface of the membrane containing negatively charged DPPG, and no NP translocation across the membrane was observed. In mode II, the NP directly translocated across the membrane; notably, the transient transmembrane pore was immediately resealed after NP translocation.[19–21] Mode II is the ideal translocation pathway. In mode III, direct translocation of the NP across the membrane was also observed; however, transmembrane pores formed after NP translocation.

Fig. 5b shows the mapping result of the three modes as a function of cholesterol content (x-axis) and the applied membrane potential $\Delta\psi_{appl}$ (y-axis). We mapped the mode of NP behavior with the highest occurrence probability among five independent runs. Each mode of the NP behavior is depicted by

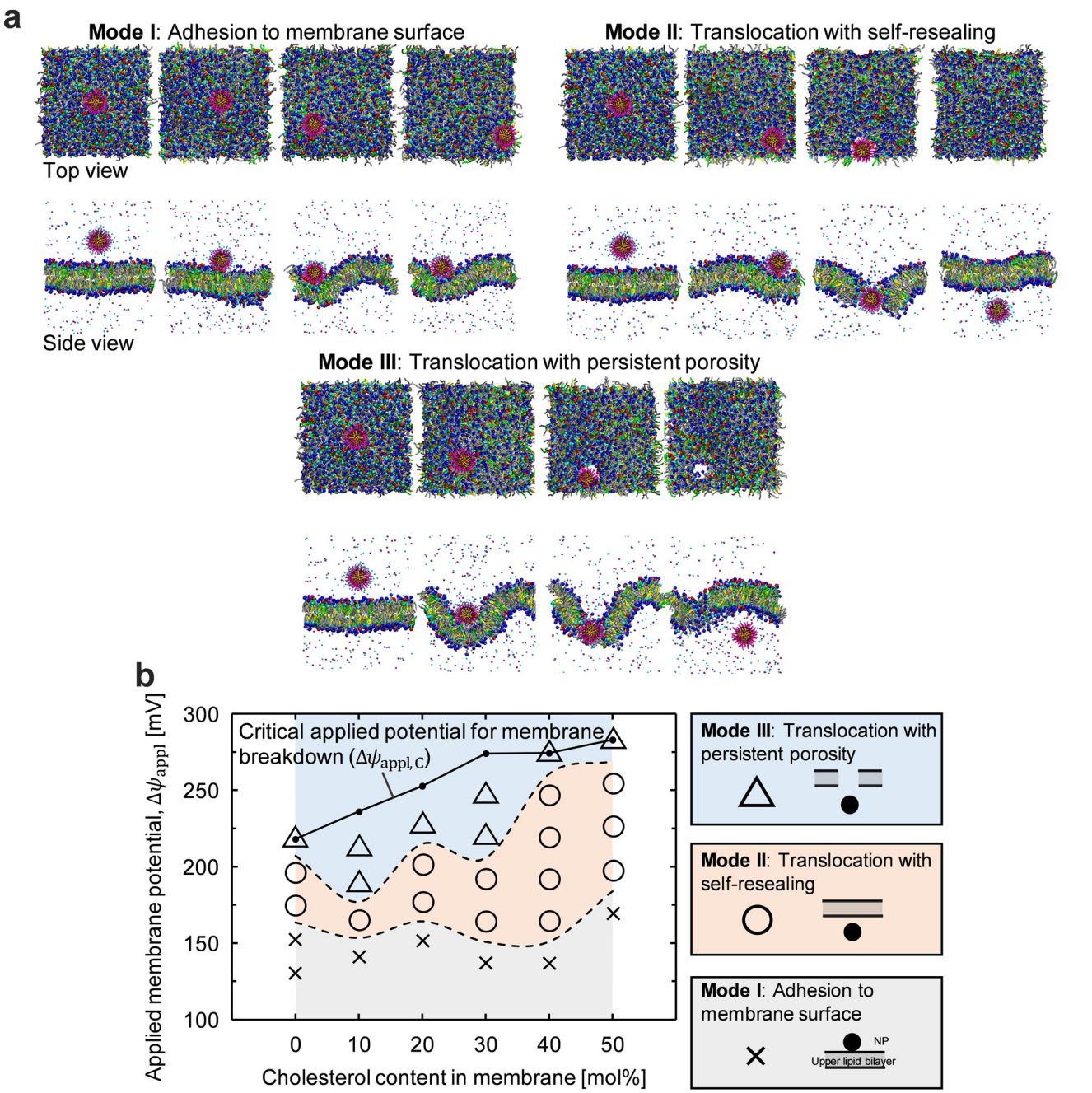

Fig. 5 (a) Three-typical modes of NP behaviors. (b) Classification diagram of representative NP behavior with respect to cholesterol content and applied membrane potential, $\Delta\psi_{appl}$.

 This journal is © the Owner Societies 2024

Open Access Article. Published on 24 July 2024. Downloaded on 5/24/2026 4:01:49 PM.
This article is licensed under a Creative Commons Attribution 3.0 Unported Licence.

different symbols and colors in Fig. 5b. The results revealed that the NP was able to translocate across the cholesterol-containing membranes. Here, it was worth noting that the width of $\Delta\psi_{appl}$ that induced the mode II behavior (circle symbols in Fig. 5b), which was an ideal translocation pathway, became wider at a higher cholesterol content. As presented in the previous section, a higher cholesterol content generally leads to a more rigid and mechanically stable lipid bilayer, owing to the cholesterol-condensing effect. Therefore, we expected that the NP would be unlikely to translocate across membranes with a higher cholesterol content. However, the results of the CG-MD simulation contradicted this expectation.

With an increase in $\Delta\psi_{appl}$, the NP behavior shifted from mode I to mode II and then to mode III at any cholesterol content. As seen in Fig. 5b, the broadening of the $\Delta\psi_{appl}$-window for mode II at a higher cholesterol content resulted from transitions in specific criteria with increasing cholesterol content. The $\Delta\psi_{appl}$-criterion between modes I and II exhibited only a slight variation as the cholesterol content increased. Conversely, the $\Delta\psi_{appl}$-criterion between modes II and III increased with a higher cholesterol content. In the next section, the behaviors of these two $\Delta\psi_{appl}$-criteria were discussed in detail by analyzing the simulation results.

To verify the aforementioned transitions of the $\Delta\psi_{appl}$-criteria obtained from the MD simulation, the membrane-crossing of NP across cholesterol-containing lipid bilayer membranes was investigated experimentally using a planar bilayer lipid membrane with the electrophysiological technique.[22] Details of the experimental method and results can be seen in the ESI† (Fig. S1, S2, and Table S1). The experimental results demonstrated qualitative agreement with the simulation in terms of the $\Delta\psi_{appl}$-criteria transitions observed in the MD simulation, thereby validating the simulation results.

Change in lipid composition at the NP–membrane contact interface

To investigate why the $\Delta\psi_{appl}$-criterion between modes I and II exhibited only a slight variation with increasing cholesterol content, we focused on changes in lipid composition at the NP–membrane contact interface.

Fig. 6a shows typical snapshots of mode II. Snapshots were taken from the side and top (positive z-axis direction) of the membrane at the onset of NP adhesion to the membrane core (27.2 ns) and immediately before NP penetration into the membrane (158.4 ns). DPPC is depicted in transparent gray. In the top view, the NP is represented by a black circle corresponding to its projected area. At the onset of NP adhesion, both cholesterol and DPPG were observed within the black circle, indicating that both cholesterol and DPPG were present at the NP–membrane contact interface. However, just before NP penetration, cholesterols existing at the contact interface were lower, whereas the DPPG-rich domain was formed at the contact interface. Fig. 6b shows the temporal change in lipid composition at the NP–membrane contact interface during NP adhesion to the membrane in mode II. The shaded areas in Fig. 6b represent periods of NP adhesion to the membrane surface (orange) and NP penetration and translocation (light gray). In this study, lipids at the NP–membrane contact interface refer to lipid molecules within 2.55 nm (NP radius +0.6 nm) from the center of mass of the NP. Fig. 6b shows that, during NP adhesion to the membrane surface, the local content of negatively charged DPPG at the contact interface increased, whereas the cholesterol content decreased. Furthermore, just before NP penetration, a rapid increase in the DPPG content and a rapid decrease in the cholesterol content were observed. The observed result indicates that the Coulombic force between the positively charged NP and the negatively charged DPPG induced a change in the local lipid composition at the NP–membrane contact interface, deviating from the whole membrane-based lipid composition.

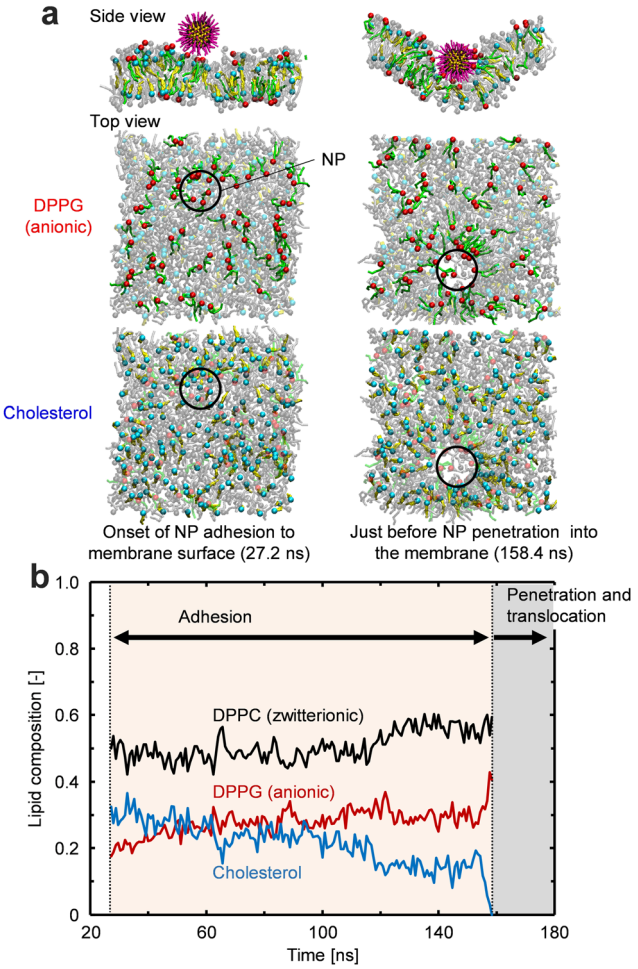

Fig. 6 (a) Side and top views of snapshots in mode II at the onset of NP adhesion to the membrane and just before NP penetration into the membrane. The DPPC molecules are depicted in transparent gray, and the projected area of the NP is denoted by a black circle. Only the outer leaflet in the upper bilayer is shown in the top views for clarity. (b) Temporal change in the local lipid composition at the NP–membrane interface in the case of a 30 mol% cholesterol content and an applied membrane potential of 165 mV. The region with a red background indicates the duration during which NP adhered to the membrane, while the region with a gray background indicates the duration during which NP penetrated the membrane.

Open Access Article. Published on 24 July 2024. Downloaded on 5/24/2026 4:01:49 PM.
This article is licensed under a Creative Commons Attribution 3.0 Unported Licence.

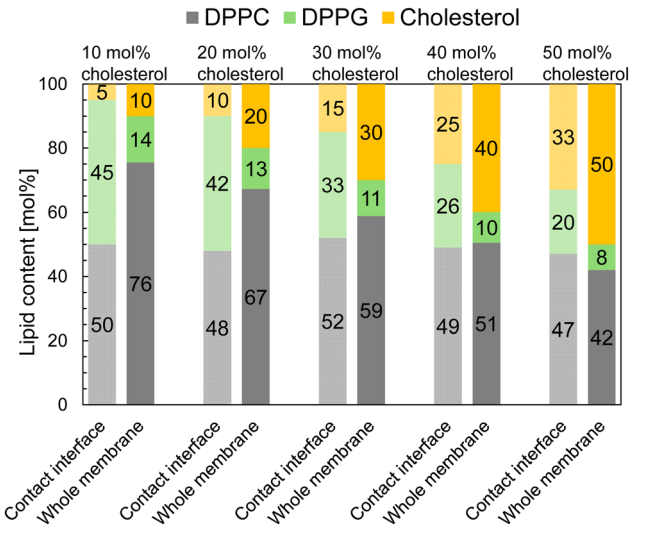

Fig. 7 Comparison between the local lipid contents at the NP–membrane contact interface just before NP penetration and those in the whole membrane. The lipid contents at the contact interface were calculated in mode II by time averaging over 5 ns just before the onset of NP penetration. The time-averaged content was further averaged over five independent runs with various initial positions of the NP.

Fig. 7 shows the comparison between the local lipid contents (cholesterol, DPPG, and DPPC) at the NP–membrane contact interface just before NP penetration and the overall lipid contents in the whole membrane. It was clearly demonstrated that the DPPG-rich/cholesterol-poor domain (as compared to the lipid contents in the whole membrane) was formed at the NP–membrane contact interface at any cholesterol contents. We speculate that this DPPG-rich/cholesterol-poor domain may be responsible for the observed invariance (0–40 mol% cholesterol) and a slight increase (40–50 mol% cholesterol) in the $\Delta\psi_{appl}$-criterion between modes I and II with increasing the cholesterol content. Further theoretical understanding and quantitative modeling are required to elucidate the quantitative relationship between the local content of ternary lipids and $\Delta\psi_{appl}$ at the NP–membrane contact interface, which is likely to be a complex nonlinear relationship. This will be the subject of future work.

Size of the pore formed in the membrane during NP translocation

To investigate why the $\Delta\psi_{appl}$-criterion between modes II and III became higher at a higher cholesterol content, the size of the pore formed in the membrane during NP translocation was analyzed. Fig. 8a shows the top view of the pore during NP translocation across the membrane. The snapshots show that the gap between the NP and lipid molecules was smaller at higher cholesterol contents (40 and 50 mol%), indicating that the NP passed through the pore consisting of more tightly packed lipid molecules at higher cholesterol contents. Fig. 8b shows the pore areas for different cholesterol concentrations. The pore area was defined as the projected area of the lipid-free region of the membrane in the top view from the positive

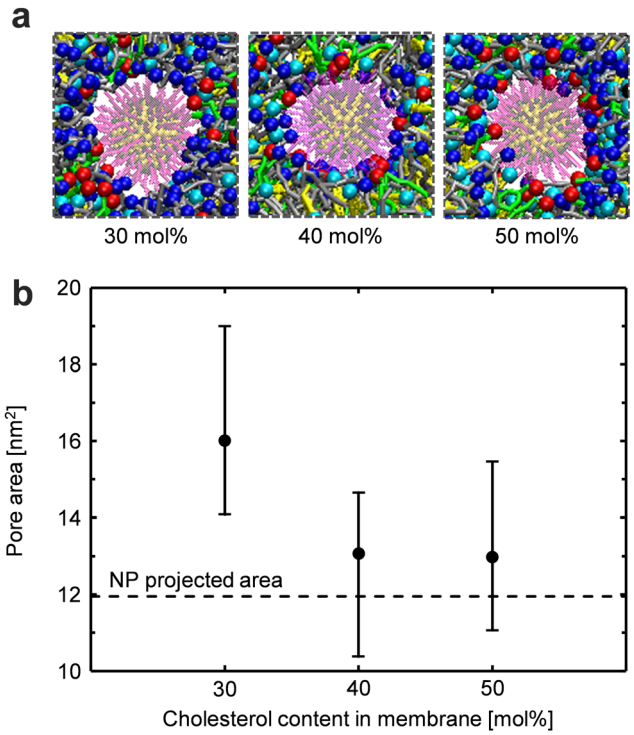

Fig. 8 (a) Top view of snapshots during NP translocation across the membrane. (b) Pore area formed during NP translocation as a function of cholesterol content in the membrane under an applied membrane potential of 165 mV. The dashed line was the projected area of the NP. The pore area was calculated as the average value of five independent runs with various initial positions of the NP. The error bars represent its maximum and minimum values.

direction of the *z*-axis.[19,21] It was confirmed that the pore area at higher cholesterol contents (40 and 50 mol%) was smaller than that at a lower cholesterol content (30 mol%). The pore areas at 40 and 50 mol% were almost equivalent to the projected area of the NP. When the pore formed during NP translocation is small, it is likely to self-reseal after NP translocation. Therefore, with an increase in cholesterol content, the membrane becomes more prone to self-resealing after NP translocation.

In summary, it was found that the NP passed through smaller transmembrane pores at higher cholesterol contents, leading to an increase in the $\Delta\psi_{appl}$-criterion between modes II and III at higher cholesterol contents.

Mechanism of NP translocation across a membrane containing cholesterol

According to the above discussion, the mechanism of NP translocation across cholesterol-containing membranes is as follows (Fig. 9). First, the positively charged NP adheres to the outer surface of the membrane owing to the electrostatic forces induced by the applied electric field and Coulombic interactions with the negatively charged membrane (Fig. 9a). Subsequently, negatively charged DPPG molecules accumulate at the NP–membrane interface owing to Coulombic attraction between them and the positively charged NP (Fig. 9b). This accumulation results

 This journal is © the Owner Societies 2024

Open Access Article. Published on 24 July 2024. Downloaded on 5/24/2026 4:01:49 PM.
This article is licensed under a Creative Commons Attribution 3.0 Unported Licence.

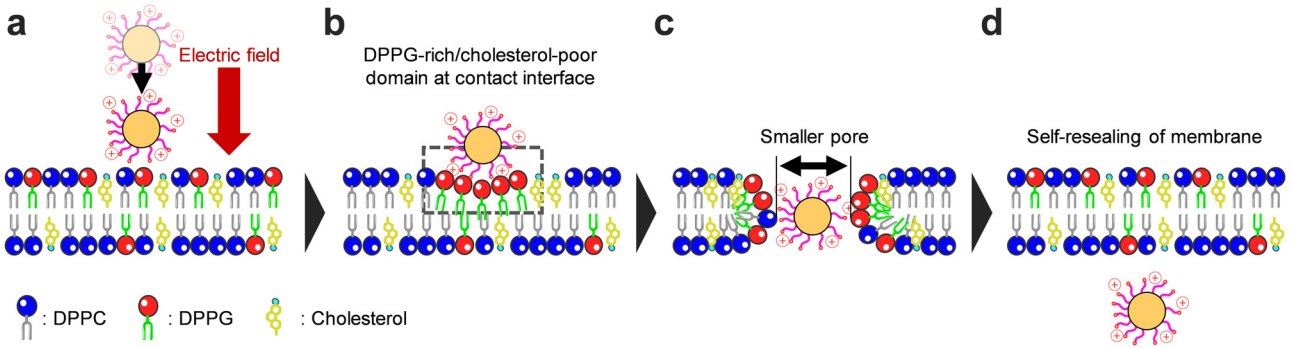

Fig. 9 Schematic of the mechanism of NP translocation across the cholesterol-containing membrane.

in a DPPG-rich/cholesterol-poor domain at the contact interface. As a result, the cholesterol-condensing effect is locally reduced at the interface as compared to the whole membrane-based condensing effect, leading to the direct translocation of the NP across the membrane, even at the cholesterol-containing membrane. Furthermore, the transmembrane pore formed during NP translocation became smaller in the cholesterol-containing membrane (Fig. 9c). After NP translocation, the small pore readily reseals, allowing for the self-resealing of the membrane (Fig. 9d).

Conclusions

In this study, we investigated the direct translocation of an NP across a cholesterol-containing lipid bilayer under an external electric field using CG-MD simulations. We found that a positively charged NP translocated directly across cholesterol-containing membranes without irreversible membrane disruption. The range of the applied membrane potential that induced this unique NP translocation mode became wider in the cholesterol-containing membranes. Two key phenomena have been identified to explain the unique effects of cholesterol. First, before the NP crossed the membrane, a DPPG-rich/cholesterol-poor domain was formed at the NP–membrane contact interface because of the Coulombic attraction between the positively charged NP and negatively charged DPPG lipids. Second, a higher cholesterol content in the membrane led to smaller transmembrane pores during NP translocation. These two key phenomena resulted in the local reduction of the cholesterol condensing effect at the contact interface and the ease of membrane self-resealing. As a result, the range of the applied membrane potential that induced membrane crossing of the NP without persistent membrane disruption expanded with a higher cholesterol content.

Author contributions

Masaya Tajima: data curation, investigation, formal analysis, methodology, visualization, writing – original draft, and writing – review and editing. Hideya Nakamura: conceptualization, formal analysis, funding acquisition, methodology, project administration, resources, supervision, visualization, and writing – review and editing. Shuji Ohsaki: resources, validation, and writing – review and editing. Satoru Watano: resources, validation, and writing – review and editing.

Data availability

The authors confirm that the data supporting the findings of this study are available within the article and its ESI.†

Conflicts of interest

There are no conflicts of interest to declare.

Acknowledgements

This study was supported by the Japan Society for the Promotion of Science (KAKENHI Grant Numbers 18H03536, 19K22976, and 19KK0129).

Notes and references

1 R. Mout, D. F. Moyano, S. Rana and V. M. Rotello, Surface functionalization of nanoparticles for nanomedicine, *Chem. Soc. Rev.*, 2012, **41**, 2539–2544.
2 L. Y. T. Chou, K. Ming and W. C. W. Chan, Strategies for the intracellular delivery of nanoparticles, *Chem. Soc. Rev.*, 2011, **40**, 233–245.
3 K. Shao, S. Singha, X. Clemente-Casares, S. Tsai, Y. Yang and P. Santamaria, Nanoparticle-based immunotherapy for cancer, *ACS Nano*, 2015, **9**, 16–30.
4 M. P. Stewart, A. Sharei, X. Ding, G. Sahay, R. Langer and K. F. Jensen, *In vitro* and *ex vivo* strategies for intracellular delivery, *Nature*, 2016, **538**, 183–192.
5 X. Zhang, G. Ma and W. Wei, Simulation of nanoparticles interacting with a cell membrane: Probing the structural basis and potential biomedical application, *NPG Asia Mater.*, 2021, **13**, 1–18.
6 D. Jaque, L. Martínez Maestro, B. Del Rosal, P. Haro-Gonzalez, A. Benayas, J. L. Plaza, E. M. Martín Rodríguez

Open Access Article. Published on 24 July 2024. Downloaded on 5/24/2026 4:01:49 PM. This article is licensed under a Creative Commons Attribution 3.0 Unported Licence.

and J. García Solé, Nanoparticles for photothermal therapies, *Nanoscale*, 2014, **6**, 9494–9530.
7 M. Laprise-Pelletier, T. Simão and M. A. Fortin, Gold nanoparticles in radiotherapy and recent progress in nanobrachytherapy, *Adv. Healthcare Mater.*, 2018, **7**, e1701460.
8 A. J. Mieszawska, W. J. M. Mulder, Z. A. Fayad and D. P. Cormode, Multifunctional gold nanoparticles for diagnosis and therapy of disease, *Mol. Pharmaceutics*, 2013, **10**, 831–847.
9 L. K. Bogart, G. Pourroy, C. J. Murphy, V. Puntes, T. Pellegrino, D. Rosenblum, D. Peer and R. Lévy, Nanoparticles for imaging, sensing, and therapeutic intervention, *ACS Nano*, 2014, **8**, 3107–3122.
10 W. Chen, S. Zhang, Y. Yu, H. Zhang and Q. He, Structural-engineering rationales of gold nanoparticles for cancer theranostics, *Adv. Mater.*, 2016, **28**, 8567–8585.
11 J. Wang, J. Sun, Y. Wang, T. Chou, Q. Zhang, B. Zhang, L. Ren and H. Wang, Gold nanoframeworks with mesopores for Raman–photoacoustic imaging and photo-chemo tumor therapy in the second near-infrared biowindow, *Adv. Funct. Mater.*, 2020, **30**, 1–13.
12 Z. Li, Y. Zhang, D. Zhu, S. Li, X. Yu, Y. Zhao, X. Ouyang, Z. Xie and L. Li, Transporting carriers for intracellular targeting delivery *via* non-endocytic uptake pathways, *Drug Delivery*, 2017, **24**(supp1), 45–55.
13 C. M. Beddoes, C. P. Case and W. H. Briscoe, Understanding nanoparticle cellular entry: A physicochemical perspective, *Adv. Colloid Interface Sci.*, 2015, **218**, 48–68.
14 E. Okoampah, Y. Mao, S. Yang, S. Sun and C. Zhou, Gold nanoparticles–biomembrane interactions: From fundamental to simulation, *Colloids Surf., B*, 2020, **196**, 111312.
15 E. Neumann, M. Schaefer-Ridder, Y. Wang and P. H. Hofschneider, Gene transfer into mouse lyoma cells by electroporation in high electric fields, *EMBO J.*, 1982, **1**, 841–845.
16 S. Huang, H. Deshmukh, K. K. Rajagopalan and S. Wang, Gold nanoparticles electroporation enhanced polyplex delivery to mammalian cells, *Electrophoresis*, 2014, **35**, 1837–1845.
17 M. Ahmadi Kamalabadi, A. Neshastehriz, H. Ghaznavi and S. M. Amini, Folate functionalized gold-coated magnetic nanoparticles effect in combined electroporation and radiation treatment of HPV-positive oropharyngeal cancer, *Med. Oncol.*, 2022, **39**, 196.
18 Y. Jiang, R. Jenjob and S. G. Yang, Enhanced therapeutic potential of irreversible electroporation under combination with gold-doped mesoporous silica nanoparticles against EMT-6 breast cancer cells, *Biosensors*, 2022, **13**, 1–11.
19 K. Shimizu, H. Nakamura and S. Watano, MD simulation study of direct permeation of a nanoparticle across the cell membrane under an external electric field, *Nanoscale*, 2016, **8**, 11897–11906.
20 H. Nakamura, K. Sezawa, M. Hata, S. Ohsaki and S. Watano, Direct translocation of nanoparticles across a model cell membrane by nanoparticle-induced local enhancement of membrane potential, *Phys. Chem. Chem. Phys.*, 2019, **21**, 18830–18838.
21 Y. Ikeda, H. Nakamura, S. Ohsaki and S. Watano, Direct translocation of a negatively charged nanoparticle across a negatively charged model cell membrane, *Phys. Chem. Chem. Phys.*, 2021, **23**, 10591–10599.
22 H. Nakamura, T. Okamura, M. Tajima, R. Kawano, M. Yamaji, S. Ohsaki and S. Watano, Enhancement of cell membrane permeability by using charged nanoparticles and a weak external electric field, *Phys. Chem. Chem. Phys.*, 2023, **25**, 32356–32363.
23 A. Das, M. S. Brown, D. D. Anderson, J. L. Goldstein and A. Radhakrishnan, Three pools of plasma membrane cholesterol and their relation to cholesterol homeostasis, *eLife*, 2014, **3**, 1–16.
24 G. Van Meer, D. R. Voelker and G. W. Feigenson, Membrane lipids: Where they are and how they behave, *Nat. Rev. Mol. Cell Biol.*, 2008, **9**, 112–124.
25 P. L. Yeagle, Cholesterol and the cell membrane, *Biochim. Biophys. Acta*, 1985, **822**, 267–287.
26 H. Ohvo-Rekilä, B. Ramstedt, P. Leppimäki and J. P. Slotte, Cholesterol interactions with phospholipids in membranes, *Prog. Lipid Res.*, 2002, **41**, 66–97.
27 M. L. Fernández, G. Marshall, F. Sagués and R. Reigada, Structural and kinetic molecular dynamics study of electroporation in cholesterol-containing bilayers, *J. Phys. Chem. B*, 2010, **114**, 6855–6865.
28 S. Koronkiewicz and S. Kalinowski, Influence of cholesterol on electroporation of bilayer lipid membranes: Chronopotentiometric studies, *Biochim. Biophys. Acta*, 2004, **1661**, 196–203.
29 P. Kramar and D. Miklavčič, Effect of the cholesterol on electroporation of planar lipid bilayer, *Bioelectrochemistry*, 2022, **144**, 108004.
30 J. Yuan and F. Meng, Effects of cholesterol on chlorzoxazone translocation across POPC bilayer, *J. Mol. Model.*, 2021, **27**, 146.
31 L. Zhang, W. F. D. Bennett, T. Zheng, P. K. Ouyang, X. Ouyang, X. Qiu, A. Luo, M. Karttunen and P. Chen, Effect of cholesterol on cellular uptake of cancer drugs pirarubicin and ellipticine, *J. Phys. Chem. B*, 2016, **120**, 3148–3156.
32 M. M. de Sá, V. Sresht, C. O. Rangel-Yagui and D. Blankschtein, Understanding miltefosine-membrane interactions using molecular dynamics simulations, *Langmuir*, 2015, **31**, 4503–4512.
33 P. Chen, I. Vorobyov, B. Roux and T. W. Allen, Molecular Dynamics simulations based on polarizable models show that ion permeation interconverts between different mechanisms as a function of membrane thickness, *J. Phys. Chem. B*, 2021, **125**, 1020–1035.
34 P. Gkeka, P. Angelikopoulos, L. Sarkisov and Z. Cournia, Membrane partitioning of anionic, ligand-coated nanoparticles is accompanied by ligand snorkeling, local disordering, and cholesterol depletion, *PLoS Comput. Biol.*, 2014, **10**, e1003917.
35 S. J. Marrink, H. J. Risselada, S. Yefimov, D. P. Tieleman and A. H. De Vries, The MARTINI force field: Coarse grained model for biomolecular simulations, *J. Phys. Chem. B*, 2007, **111**, 7812–7824.
36 S. J. Marrink, A. H. De Vries and A. E. Mark, Coarse grained model for semiquantitative lipid simulations, *J. Phys. Chem. B*, 2004, **108**, 750–760.

Open Access Article. Published on 24 July 2024. Downloaded on 5/24/2026 4:01:49 PM. This article is licensed under a Creative Commons Attribution 3.0 Unported Licence.

37 J. Lin and A. Alexander-Katz, Cell membranes open ''doors'' for cationic nanoparticles/biomolecules: Insights into uptake kinetics, *ACS Nano*, 2013, **7**, 10799–10808.
38 J. Lin, H. Zhang, Z. Chen and Y. Zheng, Penetration of lipid membranes by gold nanoparticles: Insights into cellular uptake, cytotoxicity, and their relationship, *ACS Nano*, 2010, **4**, 5421–5429.
39 S. O. Yesylevskyy, L. V. Schäfer, D. SenGupta and S. J. Marrink, Polarizable water model for the coarse-grained MARTINI force field, *PLoS Comput. Biol.*, 2010, **6**, e1000810.
40 M. N. Melo, H. I. Ingólfsson and S. J. Marrink, Parameters for Martini sterols and hopanoids based on a virtual-site description, *J. Chem. Phys.*, 2015, **143**, 243152.
41 A. Zachowski, Phospholipids in animal eukaryotic membranes: Transverse asymmetry and movement, *Biochem. J.*, 1993, **294**, 1–14.
42 S. Rana, A. Bajaj, R. Mout and V. M. Rotello, Monolayer coated gold nanoparticles for delivery applications, *Adv. Drug Delivery Rev.*, 2012, **64**, 200–216.
43 J. Lin, H. Zhang, Z. Chen and Y. Zheng, Penetration of lipid membranes by gold nanoparticles: insights into cellular uptake, cytotoxicity, and their relationship, *ACS Nano*, 2010, **4**, 5421–5429.
44 J. Lin and A. Alexander-Katz, Cell membranes open ''doors'' for cationic nanoparticles/biomolecules: insights into uptake kinetics, *ACS Nano*, 2013, **7**, 10799–10808.
45 H. Ohshima, T. W. Healy and L. R. White, Accurate analytic expressions for the surface charge density/surface potential relationship and double-layer potential distribution for a spherical colloidal particle, *J. Colloid Interface Sci.*, 1982, **90**, 17–26.
46 C. Hofsäss, E. Lindahl and O. Edholm, Molecular dynamics simulations of phospholipid bilayers with cholesterol, *Biophys. J.*, 2003, **84**, 2192–2206.
47 Y. Zhang, J. W. Carter, A. Lervik, N. J. Brooks, J. M. Seddon and F. Bresme, Structural organization of sterol molecules in DPPC bilayers: A coarse-grained molecular dynamics investigation, *Soft Matter*, 2016, **12**, 2108–2117.
48 D. P. Tieleman, The molecular basis of electroporation, *BMC Biochem.*, 2004, **5**, 10.
49 W. C. Hung, M. T. Lee, F. Y. Chen and H. W. Huang, The condensing effect of cholesterol in lipid bilayers, *Biophys. J.*, 2007, **92**, 3960–3967.
50 F. Leeb and L. Maibaum, Spatially resolving the condensing effect of cholesterol in lipid bilayers, *Biophys. J.*, 2018, **115**, 2179–2188.
51 D. Van Der Spoel, E. Lindahl, B. Hess, G. Groenhof, A. E. Mark and H. J. Berendsen, GROMACS: Fast, flexible, and free, *J. Comput. Chem.*, 2005, **26**, 1701–1718.
52 W. Humphrey, A. Dalke and K. Schulten, VMD, VMD: Visual Molecular Dynamics, *J. Mol. Graphics*, 1996, **14**, 33–38.
53 M. Parrinello and A. Rahman, Polymorphic transitions in single crystals: A new molecular dynamics method, *J. Appl. Phys.*, 1981, **52**, 7182–7190.
54 G. Bussi, D. Donadio and M. Parrinello, Canonical sampling through velocity rescaling, *J. Chem. Phys.*, 2007, **126**, 014101.
55 Z. C. Y. Wang, P. Gkeka, J. E. Fuchs and K. R. Liedl, *Biochim. Biophys. Acta, Rev. Biomembr.*, 2016, **11**, 2846–2857.
56 I. van Uitert, S. Le Gac and A. van den Berg, The influence of different membrane components on the electrical stability of bilayer lipid membranes, *Biochim. Biophys. Acta*, 2010, **1798**, 21–31.
57 J. Czub and M. Baginski, Comparative Molecular Dynamics study of lipid membranes containing cholesterol and ergosterol, *Biophys. J.*, 2006, **90**, 2368–2382.
58 R. D. Shannon, Revised effective ionic radii and systematic studies of interatomise distances in halides and Chaleogenides, *Acta Crystallogr.*, 1976, **A32**, 751–767.